Resonant weak-value enhancement for solid-state quantum metrology

Mahadevan Subramanian,[1] Amal Mathew,[1,†] and Bhaskaran Muralidharan[2,3,*]

[1] *Department of Physics, Indian Institute of Technology Bombay, Powai, Mumbai 400076, India*
[2] *Department of Electrical Engineering, Indian Institute of Technology Bombay, Powai, Mumbai 400076, India*
[3] *Centre of Excellence in Quantum Information, Computation, Science and Technology, Indian Institute of Technology Bombay, Powai, Mumbai 400076, India*

(Received 19 January 2023; revised 24 May 2023; accepted 26 September 2023; published 25 October 2023)

Quantum metrology that employs weak values can potentially effectuate parameter estimation with an ultrahigh sensitivity and has been typically explored across quantum optics setups. Recognizing the importance of sensitive parameter estimation in the solid state, we propose a spintronic device platform to realize this. The setup estimates a very weak localized Zeeman splitting by exploiting a resonant tunneling-enhanced magnetoresistance readout. We establish that this paradigm offers nearly optimal performance with a quantum Fisher information enhancement of about 10^4 times that of single high-transmissivity barriers. The obtained signal also offers a high sensitivity in the presence of dephasing effects typically encountered in the solid state. These results put forth definitive possibilities in harnessing the inherent sensitivity of resonant tunneling for solid-state quantum metrology with potential applications, especially, in the sensitive detection of small induced Zeeman effects in quantum material heterostructures.

DOI: 10.1103/PhysRevApplied.20.044065

I. INTRODUCTION

Quantum metrology [1–3] provides the means toward high-sensitivity parameter estimation using a quantum state as a probe, followed by measurements, and has been demonstrated in a variety of systems [4–9]. It is also well established that weak values can inextricably be linked with quantum sensing [10–12]. The use of weak values in quantum sensing has typically been explored using quantum optics setups [13–16]. An important metric to benchmark the quantum sensor performance is the quantum Fisher information (QFI) [17–20], which can also be linked to weak values [10]. The enhancement of weak values has shown clear experimental advantages for quantum sensing, as demonstrated in many works [21–23], despite theoretical studies which point to how postselection is disadvantageous, mainly because of a loss in QFI [24,25]. This discrepancy has been explored thoroughly with ways to surmount these disadvantages [26,27] and methods to increase detection probability as well [28].

Solid-state setups have recently garnered a lot of attention as pivotal testbeds for foundational quantum concepts, such as quantum state tomography of electrons [29,30], entanglement generation by Cooper-pair splitting [31–35], and even loophole-free Bell test experiments [36–38]. Given recent advancements in quantum materials and devices, there exist numerous applications that a quantum sensor could provide with its inherent quantum advantage, which includes the detection of induced Zeeman splitting in van der Waals heterostructures [39–45], and the precise estimation of the Rashba spin-orbit coupling parameter [46,47], to name but two. In this paper, we demonstrate how double-barrier resonant tunneling in the solid state can be exploited for high-sensitivity detection of localized Zeeman splittings due to an enhanced weak value, via a magnetoresistance measurement.

The setup we propose builds on a generalized four-terminal spin-transport setup [43–45]. The magnetoresistance measurement is directly related to a weak value A_w [48,49] of a spatial operator $\hat{A}$ which is defined using the barrier and region of the Zeeman splitting. Here $|i\rangle$ is a preselected state and $|f\rangle$ is the postselected state which gives the weak value

$$A_w = \frac{\langle f|\hat{A}|i\rangle}{\langle f\ |i\rangle}. \tag{1}$$

We now refer to Fig. 1(a), in order to demonstrate how our approach for enhancing weak values differs from the general approach of postselecting $|f\rangle$ for a small $\langle f\ |i\rangle$ [25].

By the nature of our setup, the only control we have is changing the incident wave vector which defines $|i\rangle$ as the energy eigenvector of the spin-independent barrier and $|f\rangle$ being a spatial wave function of the same energy which is nonzero only to the right of the barriers. The choice corresponding to the resonant tunneling wave vectors has

*bm@ee.iitb.ac.in
†Present address: Department of Applied Physics, Stanford University, Stanford, California 94305, USA.

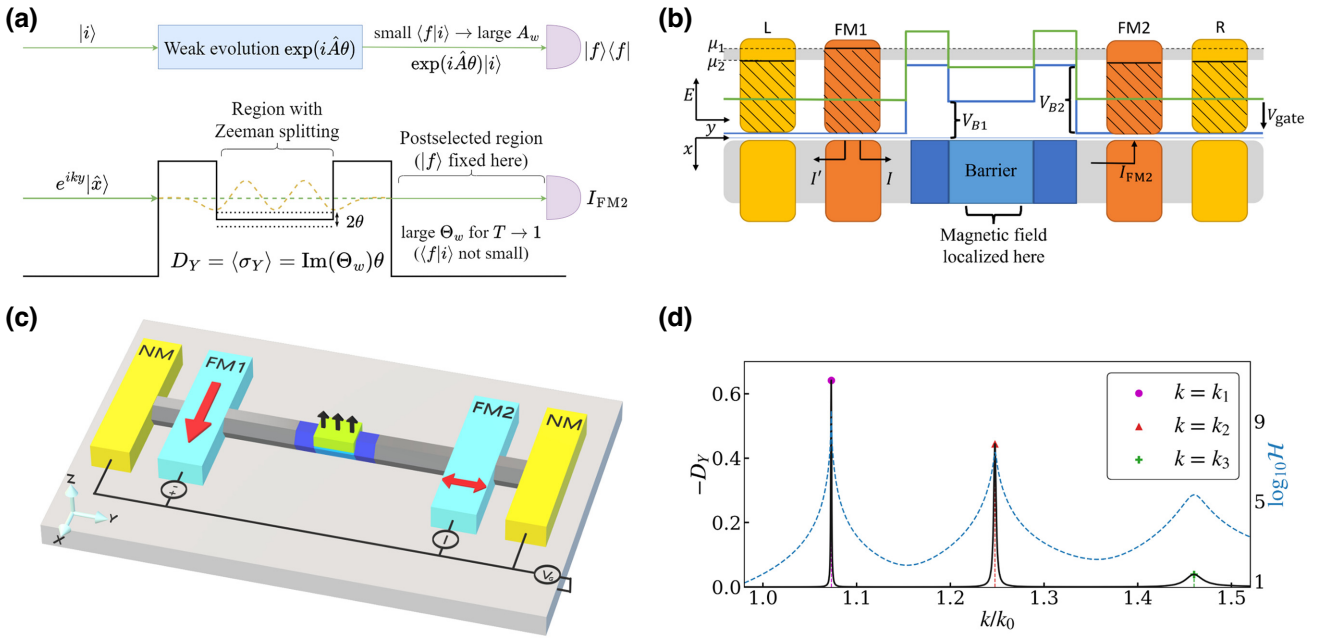

FIG. 1. Preliminaries and magnetoresistance signal. (a) A simple schematic (top) representing the weak value, and the sensing task (bottom) for estimating any localized Zeeman splitting inside the resonant tunneling barrier. General weak-value enhancement techniques involve postselecting a state $|f\rangle$. Our setup features an enhancement of the weak value A_w by varying the initial state via a choice of the wave vector k. Contrary to typical setups, the weak value is enhanced via a choice of $|i\rangle$ although $\langle f \mid i\rangle$ is not small in general. Here Θ_w is the weak value associated with the barrier. (b) Detailed device schematic with description of the embedded barrier region. The bottom gate voltage tunes a specific k value via a gate potential V_{gate} and a small bias voltage $\mu_1 - \mu_0$ selects out the outgoing stream. (c) Device schematic for the one-dimensional (1D) channel. There are four contacts, two normal metallic (NM) contacts (colored yellow) and two ferromagnetic (FM) contacts (colored blue) in the direction depicted by the red arrows. Current readings are obtained from the contact FM2. (d) A summit result depicting the signal D_Y as a function of k plotted along with the QFI, shown as $\log_{10}\mathcal{H}$. We note that there are three characteristic peaks for the k values for which resonant tunneling occurs, k_1, k_2, and k_3, which are also values where the QFI takes large values.

the largest weak-value despite having the largest $\langle f \mid i\rangle$ overlap via close-to-unity transmission. Our approach provides means to enhance both the weak values in tandem with increasing sensitivity, via an enhancement in the QFI. We make use of resonant tunneling energy channels [50] using a double-barrier setup [51–53], schematized in Figs. 1(b) and 1(c), thereby allowing Fabry-Perot resonances at specific energies. We also quantify our design with the QFI and further analyze the effects of phase breaking [49,54–63] that are typically detrimental in such solid-state systems.

II. FORMULATION AND TRANSPORT SETUP

A few intertwining concepts need to be expanded upon at this stage, as we introduce, investigate, and evaluate the proposal.

A. Weak values and sensing

We first connect the spin-dependent tunneling problem with the concept of weak values. We examine a 1D spin-dependent Hamiltonian of form $\hat{H} = \hat{H}_0\mathbb{I} + \theta\hat{H}_1\hat{\sigma}_Z$, where $\hat{H}_0$ and $\hat{H}_1$ are the 1D spatial Hamiltonians without spin, $\mathbb{I}$ is the identity matrix, and $\hat{\sigma}_Z$ is the Pauli z matrix, respectively. In the steady state, the wave functions are obtained on solving the 1D scattering problem of the Hamiltonian with a constant flux of $\hat{x}$-polarized electrons to the left of the barrier. As for the treatment of electrons in a Larmor clock [64], the up-spin and the down-spin components of the wave function can be solved separately as solutions of $\hat{H}_0 + \theta\hat{H}_1$ and $\hat{H}_0 - \theta\hat{H}_1$, respectively.

The term $\hat{H}_0\mathbb{I}$ can be treated as a bare Hamiltonian with the localized $\theta\hat{H}_1\hat{\sigma}_Z$ being a scattering potential. Let $|\psi\rangle$ be an eigenstate of $\hat{H}_0$ with an energy $\varepsilon(k)$ and $|\psi^{\pm}\rangle$ be the scattered wave function obtained for the Hamiltonian $\hat{H}_0 \pm \theta\hat{H}_1$. Using scattering theory, the scattered waves can be calculated using the equilibrium Green's function $\hat{G}_0$ evaluated from $\hat{H}_0$ [65,66]. The expectation value $\langle\hat{\sigma}_Y\rangle$ in the region to the right of the barrier comes out to be the following up to the first order in θ (see the detailed discussion in Appendix A):

$$\langle\hat{\sigma}_Y\rangle = -2\theta\mathrm{Im}\left(\frac{\langle f|\hat{G}_0\hat{H}_1|\psi\rangle}{\langle f \mid \psi\rangle}\right) + \mathcal{O}(\theta^2). \qquad (2)$$

This equation demonstrates that a certain transport signal indicative of the parameter θ has a clear dependence on a weak value of a spatial operator.

Weak values can generally be treated via a perturbative approach [3,12,67]. For an operator $\hat{A}$, the nth-order weak value is defined to be $A_w^n = \langle f|\hat{A}^n|i\rangle/\langle f\,|\,i\rangle$, where $|i\rangle$ is the initial state and the postselection is done with state $|f\rangle$. We define $P = |\langle f\,|\,i\rangle|^2$ and $P_\epsilon = |\langle f|\hat{U}|i\rangle|^2$, where $\hat{U} = \exp\left(-i\epsilon\hat{A}\right)$. We can treat ϵ as a small parameter and perform a Taylor expansion for U and obtain

$$\frac{P_\epsilon}{P} = 1 + 2\epsilon \mathrm{Im}A_w - \epsilon^2[\mathrm{Re}A_w^2 - |A_w|^2] + \mathcal{O}(\epsilon^3). \quad (3)$$

To ensure the validity of the weak-interaction regime, the quantity $2\epsilon \mathrm{Im}A_w$ must be much larger in magnitude than the sum of all the higher-order corrections that follow, which puts a limit to increasing the sensitivity using weak values [68].

This elucidates that amplifying the imaginary part of the weak value for $\hat{G}_0\hat{H}_1$ can boost the sensitivity of $\langle\hat{\sigma}_Y\rangle$ with respect to θ as long as we are in the appropriate regime which keeps the response linear. This weak value also has physical relevance as a form of the tunneling time, as explored in Ref. [48]. It has been established that $\langle\hat{\sigma}_Y\rangle = -\omega_L\tau_Y$, where ω_L is the Larmor frequency and τ_Y is the real part of the weak value of the barrier potential [48,49], which can be proven to be equivalent to Eq. (2). This notion can be generalized in the case of more complicated barriers, which would only change the Green's function $\hat{G}_0$, while $\hat{H}_1$ takes into account the localized Zeeman splitting.

B. The magnetoresistive setup

The device setup schematized in Figs. 1(b) and 1(c) consists of a long 1D nanowire with an embedded barrier region, facilitated electrostatic gating. The embedded region consists of three rectangular barriers with heights V_{B2}, V_{B1}, and V_{B2}, with the total width being d_2 and the width of the middle region being d_1. The middle region features a magnetic field B along $\hat{z}$, which models, for instance, a weak Zeeman splitting that is to be estimated precisely, denoted by $V_Z = g\mu_B B$ (where g is the gyromagnetic ratio and μ_B is the Bohr magneton). This multiterminal setup is a 1D proof of concept, which is quite realizable using 1D nanowires or two-dimensional structures with multiple gates [43–45], and has been quite intensely pursued [43–45], especially in situations where induced Zeeman effects occur in localized regions.

We can now define the channel Hamiltonian as follows:

$$\hat{H} = \begin{cases} (\hat{p}^2/2m + V_{B1})\mathbb{I} - (V_Z/2)\hat{\sigma}_Z, & |y| \le d_1/2, \\ (\hat{p}^2/2m + V_{B2})\mathbb{I}, & d_1/2 < |y| \le d_2/2, \\ (\hat{p}^2/2m)\mathbb{I}, & |y| > d_2/2, \end{cases} \quad (4)$$

where $\theta t_0 = V_Z/2$. The Zeeman splitting is only in the region where $\hat{H}_1$ is nonzero. As depicted in Fig. 1(a), the incident beam of electrons is $+\hat{x}$ spin-polarized. The expectation value $\langle\hat{\sigma}_Y\rangle$ gives us a signal in relation to θ that depicts the precession of the spin, as previously discussed. Our simulations are conducted with the following parameters: hopping energy $t_0 = 3.875$ eV, $V_{B1} = t_0/5$, $V_{B2} = t_0/10$, $d_1 = 40$ nm, and $d_2 = 80$ nm. The single-barrier setup used for comparison has the same value of V_{B1} but $V_{B2} = 0$ and $d_1 = d_2 = 40$ nm instead, and hence it only has a single barrier in which the localized Zeeman splitting is contained. The Hamiltonian is truncated to be defined over 64 sites in a way where the barrier spans across 40 sites exactly. This further means all the matrices we deal with are truncated to be defined over exactly 64 sites.

We employ two normal metallic (NM) contacts on the ends of the channel to manipulate reflections in order to make the correct postselection and the detection of the transport signal feasible [49]. The ferromagnetic (FM) contact FM1 introduces $\hat{x}$-polarized electrons facilitated via the bias situation. The current readouts are taken at the ferromagnetic contact FM2. The alignment of FM2 is along the $\pm\hat{y}$ direction. We denote the current readout from FM2 in the $\pm\hat{y}$ direction as $I^{\pm}_{\mathrm{FM2}}$.

C. Transport formulation

To model the terminal current readout at FM2, we employ the Keldysh nonequilibrium Green's function (NEGF) technique [55,56,69,70], whose specific implementation for related setups is elaborated in the appendix of Ref. [49]. We go over the brief procedure as follows. The electron correlator is defined as $\mathbf{G}^n = -i\mathbf{G}^< = \mathbf{G}^r\mathbf{\Sigma}^{\mathrm{in}}\mathbf{G}^a$, where $\mathbf{G}^<$ is the *lesser* Green's function. Here, the retarded Green's function, $\mathbf{G}^r = [E - \hat{H} - \mathbf{\Sigma}]^{-1}$, where $\hat{H}$ is the channel Hamiltonian, $\mathbf{\Sigma}$ is the sum of all self-energies, and $\mathbf{\Sigma}^{\mathrm{in}}$ is the in-scattering function. The quantity $\mathbf{G}^a$ is the Hermitian conjugate of $\mathbf{G}^r$ [62]. The terminal currents are then defined as $I^{\pm}_{\mathrm{FM2}} = \mathrm{Tr}(\Gamma^{\pm}_{\mathrm{FM2}}\mathbf{G}^n)$. For a $\pm\hat{y}$-polarized contact, the expression for the broadening function $\Gamma^{\pm}_{\mathrm{FM2}}$ is a matrix that is only nonzero in the submatrix for the position of the FM2 contact on the channel, where it takes on value $-t_0 e^{ika}(\mathbb{I} + \hat{\sigma}_Y)/2$. Given that $\rho = \mathbf{G}^n/\mathrm{Tr}(\mathbf{G}^n)$, current measurements of $I^{\pm}_{\mathrm{FM2}}$ are proportional to the probabilities for $\pm\hat{y}$ polarization at the position of the FM2 contact, as is apparent from the form of its expression.

We now define our primary magnetoresistance signal, D_Y, which is obtained out of the current readouts from the contact FM2 when it is $\pm y$-polarized and defined as

$$D_Y = \frac{I^+_{\mathrm{FM2}} - I^-_{\mathrm{FM2}}}{I^+_{\mathrm{FM2}} + I^-_{\mathrm{FM2}}} = \langle \hat{\sigma}_Y \rangle. \tag{5}$$

From our physical understanding of the current measurements, the signal D_Y is proportional to the average value $\langle \hat{\sigma}_Y \rangle$ for the wave function on the right of the barrier. Using Eq. (2) we can directly see how D_Y can be used for detection of θ using the obtained value to estimate θ assuming linear response. We can quantify the accuracy of such estimates using the QFI.

D. Quantum Fisher information

The task of quantum sensing is fundamentally a parameter estimation task and the QFI is a very relevant figure of merit [17,18]. In a general estimation task, a set of measurements is performed on a parameterized state to retrieve information on the parameters. We focus on the single-parameter case, relevant to our setup. The symmetric logarithm derivative [20,71], denoted as $\hat{L}_\theta$, for the estimation task for a parameterized state ρ_θ is defined by the equation $\partial_\theta \rho_\theta = \frac{1}{2}(\hat{L}_\theta \rho_\theta + \rho_\theta \hat{L}_\theta)$. The QFI, denoted by $\mathcal{H}$, is defined as $\mathcal{H} = \mathrm{Tr}(\hat{L}^2_\theta \rho_\theta)$.

Given $\partial_\theta \rho_\theta$ and ρ_θ, we can find $\hat{L}_\theta$ as a solution to a continuous Lyapunov equation [71]. As established in the previous section, we can write the density matrix $\rho = \mathbf{G}^n/\mathrm{Tr}(\mathbf{G}^n)$. We define the parameter to estimate as θ where $V_Z = 2\theta t_0$. From this, we can use the NEGF equations to obtain the following expression in the lack of dephasing effects (see Appendix B for detailed discussion):

$$\partial_\theta \rho = \left(\hat{H}_1 \mathbf{G}^r - \frac{\mathrm{Tr}((\hat{H}_1 \mathbf{G}^r)\mathbf{G}^n)}{\mathrm{Tr}(\mathbf{G}^n)} \mathbb{I} \right) \rho + \rho \left((\hat{H}_1 \mathbf{G}^r)^\dagger - \frac{\mathrm{Tr}(\mathbf{G}^n (\hat{H}_1 \mathbf{G}^r)^\dagger)}{\mathrm{Tr}(\mathbf{G}^n)} \mathbb{I} \right). \tag{6}$$

This expression for $\partial_\theta \rho$ and knowledge of ρ is enough to derive the expression for the symmetric logarithmic derivative (SLD) $\hat{L}$ by simply finding the matrix elements in the eigenbasis of ρ. The classical Fisher information (CFI) [19] for this parameterized state can also be obtained by using the current measurements $I^\pm_{\mathrm{FM2}}$ to define a classical probability distribution, since currents at the FM2 contact behave like a positive operator-valued measure (POVM) for measurements along $+\hat{y}$ and $-\hat{y}$ directions (see Appendix C). Since we obtain current measurements from the contact, they will be in the ratio of the probabilities obtained from this POVM, which can be used for ascertaining the CFI. A detailed discussion on the CFI can be found in Appendix D.

We denote the CFI as $\mathcal{H}_c$, which is dependent on the POVM set that is chosen. The QFI can be equivalently defined as the maximal CFI over all POVMs, hence $\mathcal{H}_c \leq \mathcal{H}$ [17]. The quantum Cramér-Rao bound [72,73] gives us a minimum bound on $\Delta\hat{\theta}$, where $\hat{\theta}$ is an unbiased estimator for θ for M repetitions of the measurements. Picking a better POVM will result in a better $\mathcal{H}_c$, which gives a better bound on $\Delta\hat{\theta}$, as seen by the inequality

$$(\Delta\theta)^2 \geq \frac{1}{M\mathcal{H}_c} \geq \frac{1}{M\mathcal{H}}. \tag{7}$$

Another common metric for the performance is that of the signal-to-noise ratio [74]. This is linked to the QFI using a measure defined as $R_\theta = \theta^2/\Delta\theta$. From Eq. (7), we get $R_\theta \leq M\theta^2\mathcal{H}$. The quantity $\theta^2\mathcal{H}$ is also referred to as the estimability of the parameter [18]. Our setup has practically unlimited repeated measurements since we obtain steady-state current measurements. Since our signal is proportional to our parameter and the measurements are uncorrelated, R_θ would scale linearly with N with N probes. In what is known as the Heisenberg limit, the scaling of R_θ goes as N^2, which is not possible here since that would require correlations between the probes [75–77].

III. RESULTS

The signal $-D_Y$ obtained for a Zeeman splitting of $V_Z = t_0/5000$ (or $\theta = 1/10\,000$) is depicted in Fig. 1(d) and this shows us three values of the wave vector k where the signal is very clearly amplified. These wave vectors k_1, k_2 and k_3 correspond to solutions where the transmission is exactly equal to 1. By solving the 1D Schrödinger equation for the barrier potential defined in Eq. (4), we obtain boundary conditions for continuity and differentiability of the spatial wave function along the y direction. These are at the boundaries present for the four values of y equal to $\pm d_2/2$

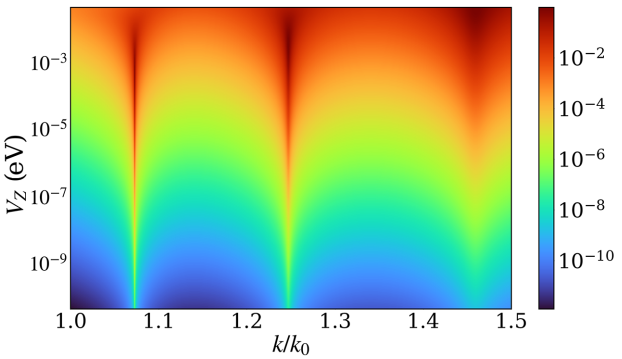

FIG. 2. Resonant enhancement in the transport signal. The contour plot depicts the dependence of the signal D_Y with respect to the Zeeman splitting energy V_Z. The signal is significantly amplified at the resonant tunneling wave vectors, as can be seen by the two sharp peaks in the contour.

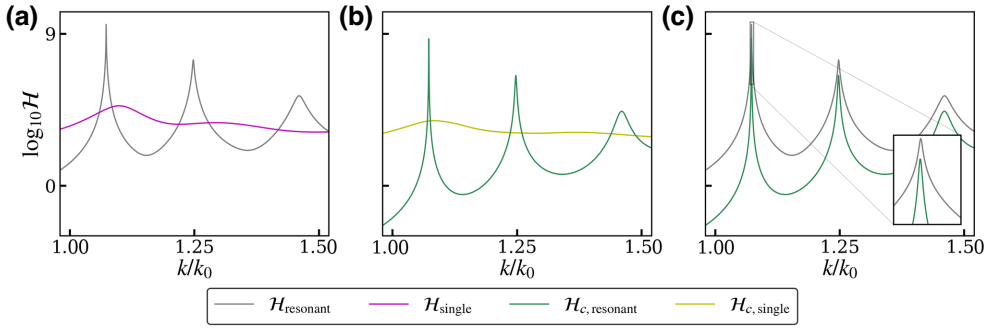

FIG. 3. QFI and CFI of the parameterized state in the setup. (a) Comparison of QFI for resonant tunneling setup to the QFI for the single-barrier setup (labeled $\mathcal{H}_{\text{single}}$). It can be seen that the resonant tunneling setup clearly outperforms the single-barrier setup near the resonant tunneling wave vectors. (b) Comparison between the CFI of the resonant tunneling setup and the single-barrier setup $\mathcal{H}_{c,\text{single}}$, again demonstrating that the resonant tunneling setup outperforms the single-barrier setup even here. (c) Comparison between the CFI (labeled $\mathcal{H}_{c,\text{resonant}}$) and the QFI of the resonant tunneling setup. We note that the CFI almost approaches the QFI for resonant tunneling wave vectors (see inset for k_1).

and $\pm d_1/2$. On solving these conditions along with setting a zero reflection at $y = -d_2/2$, and all transmission for $y > d_2/2$ (assuming an incoming wave from the left), we get a total eight equations. While there are infinite solutions to this set of equations, the two lowest-energy solutions are bound states k_1 and k_2 and correspond to resonant tunneling. The wave vector k_3 has a higher energy than V_{B2}, which does not correspond to resonant tunneling. We do not consider the higher-energy full transmission solutions since parabolic dispersion approximations fail at higher energies, within the tight-binding framework. Additionally, we plot the QFI $\mathcal{H}$ and note that, at the same values of k, the QFI is much larger, which ascertains that they can perform better sensing as well. We further explore how the signal $-D_Y$ varies with V_Z to understand its response in Fig. 2.

The three values of the wave vector k where the signal has a much higher proportionality with the Zeeman splitting is depicted in Fig. 2. However, for values of $V_Z > 10^{-3}$ eV, it can be seen that the response stops being linear, as can be noted from Fig. 2. The value of $-D_Y$ actually begins to dip for k_1 after it hits the maximum possible value of 1. To understand the response in this range would require taking into account the effects of higher orders of $\theta = V_Z/t_0$ in our signal [3,12,67].

We also compare the QFI with the CFI in Fig. 3. From these results, we can infer that, at the resonant tunneling wave vectors, $\mathcal{H}_c$ is closest to $\mathcal{H}$ which is closest to the maximum value it can possibly attain [see Fig. 3(c)]. Another inference is that our modified barrier setup outperforms the single-barrier setup by a very large margin at the resonant tunneling wave vectors [see Figs. 3(a) and 3(b)]. This shows that our sensor has the potential to give estimates with a near-optimal error margin.

Solid-state systems are prone to dephasing interactions, typically categorized as pure-phase, phase plus momentum, and spin relaxations. The dephasing interactions that arise for pure-phase relaxation are usually electron-electron interactions. The interactions for phase plus momentum relaxation are via fluctuating local nonmagnetic impurities, and those for spin relaxation are via magnetic impurities. These can be accounted for in the Keldysh NEGF method by adding the appropriate self-energies [49,54–63].

We define a scattering self-energy and the related in-scattering self-energy in the following matrix form [62,78]:

$$[\mathbf{\Sigma}_s^{r/<}]_{ij} = D_{iajkl}[\mathbf{G}^{r/<}]_{kl}. \tag{8}$$

Here D_{ijkl} is a rank-four tensor which describes the spatial correlation between impurity scattering potentials [62].

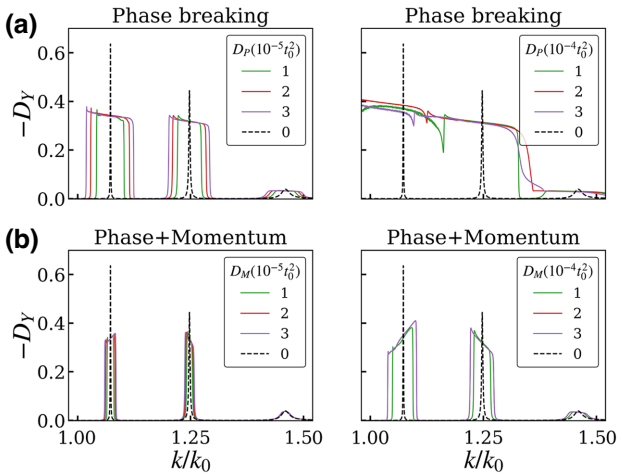

FIG. 4. Effects of phase relaxation and momentum relaxation. (a) Results for the resonant tunneling setup with nonzero values of D_P which cause pure-phase dephasing. (b) Results with nonzero values of D_M which cause phase plus momentum relaxation.

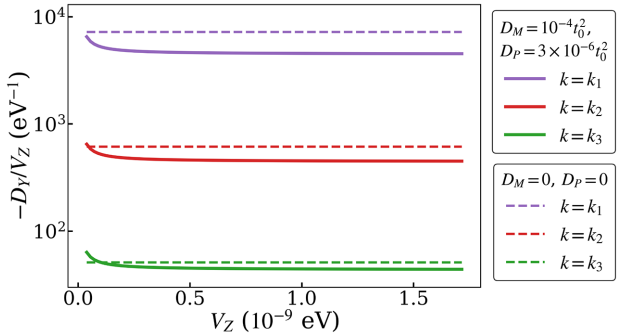

FIG. 5. Magnetoresistance signal with pure-phase relaxation and momentum relaxation. The graph shows the ratio between D_Y and V_Z, showing that the response is not perfectly linear like in the absence of dephasing. The curves become almost perfectly linear beyond a certain value of V_Z.

For pure-phase dephasing interactions, the tensor takes the following form characterized by interaction strength D_P as $D_{ijkl} = D_P\delta_{ik}\delta_{jl}$, where δ_{ij} is the Kronecker delta function. The corresponding tensor for momentum dephasing with strength D_M is $D_{ijkl} = D_M\delta_{ij}\,\delta_{ik}\delta_{jl}$.

The self-energies are then evaluated under the self-consistent Born approximation [62]. It must be noted that both of these interactions do not affect spin, and hence do not affect the measurement setup. Accounting for spin dephasing effects will destroy the signal since the setup is heavily dependent on spin coherence [49]. Figure 4 depicts the simulation results for both pure-phase and momentum dephasing. Both of these effects broaden the peaks, as would be expected, but there are qualitative differences between the two, as one can see in the graphs. Figure 5 shows the results of simulating a channel with $D_M = 10^{-4}t_0^2$ and $D_P = 3\times10^{-6}t_0^2$, which correspond to typical impurity strengths encountered in 1D channels. The linear behavior fails if we go below a Zeeman splitting less than 10^{-9} eV. There is a reduction in the slopes of this linear behavior compared to the slopes for the signals given by a clean channel. This reduction is not too large and still has the slope of the same order as can be deduced from Fig. 5.

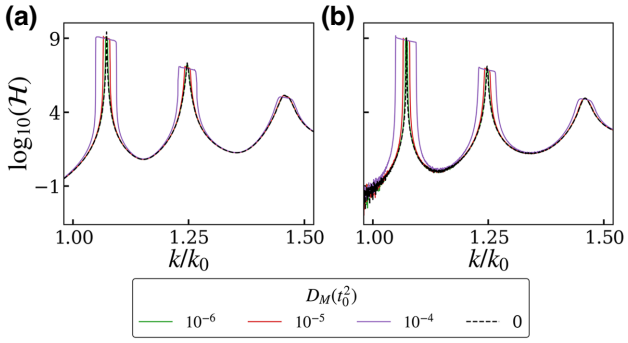

FIG. 6. Effects of phase and momentum relaxation. The graphs are (a) quantum Fisher information and (b) classical Fisher information, obtained with nonzero values of D_M which cause phase plus momentum relaxation.

IV. CONCLUSION

We have proposed a spintronic device platform to realize weak-value enhanced quantum sensing. The setup estimates a very weak localized Zeeman splitting by exploiting a resonant tunneling-enhanced magnetoresistance readout. We established that this paradigm offers a nearly optimal performance with a quantum Fisher information enhancement of about 10^4 times that of single high-transmissivity barriers. The obtained signal also offers a high sensitivity in the presence of dephasing effects typically encountered in the solid state. These results, we believe, put forth definitive possibilities in harnessing the inherent sensitivity of resonant tunneling for solid-state quantum metrology with potential applications, especially, in the sensitive detection of small induced Zeeman effects [43–45] in quantum material heterostructures.

ACKNOWLEDGMENTS

The authors acknowledge Kerem Camsari, Saroj Dash, and Sai Vinjanampathy for useful discussions. B.M. wishes to acknowledge financial support from Science and Engineering Research Board (SERB), Government of India, under Grant No. MTR/2021/000388, and Ministry of Human Resource Development (MHRD), Government of India, Grant No. STARS/APR2019/NS/226/FS under the STARS scheme.

APPENDIX A: ONE-DIMENSIONAL SCATTERING AND WEAK VALUES

We define the Hamiltonian of electrons in terms of spatial Hamiltonians $\hat{H}_0$ and $\hat{H}_1$ and some small dimensional parameter θ as

$$\hat{H} = \hat{H}_0 \otimes \mathbb{I} + \theta\hat{H}_1 \otimes \hat{\sigma}_Z. \tag{A1}$$

We now proceed to study the spectrum of scattering states with this Hamiltonian. We define a purely spatial scattering state $|\psi\rangle$ as follows:

$$\hat{H}_0\,|\psi\rangle = \varepsilon\,|\psi\rangle\,. \tag{A2}$$

This will get scattered further due to $\theta\hat{H}_1 \otimes \hat{\sigma}_Z$ in the Hamiltonian in Eq. (A1). Let $|\psi_\pm\rangle$ be the spatially scattered states for the up-spin and the down-spin channels,

respectively, expressed as

$$|\psi_\pm\rangle = |\psi\rangle \pm \frac{\theta \hat{H}_1}{\varepsilon - \hat{H}_0}\,|\psi_\pm\rangle = |\psi\rangle \pm \hat{G}_0(\varepsilon)\theta\hat{H}_1\,|\psi_\pm\rangle\,. \tag{A3}$$

Here $\hat{G}_0$ is the equilibrium isolated Green's function of the Hamiltonian $\hat{H}_0$. By the general convention, the Green's function is defined as $\hat{G}_0(\varepsilon) = [\varepsilon - \hat{H}_0 \pm i\eta]^{-1}$, with the plus and minus choice representing the retarded or the advanced Green's function, respectively. This choice will be largely irrelevant to how we use this operator, since it is never acts on an energy eigenstate directly. For the sake of convention, all mentions of $\hat{G}_0$ will be of the retarded Green's function which has greater physical relevance [66].

We define $|f\rangle$ as the part of $|\psi\rangle$ after scattering [48]. If we assume that the incident wave is $|\psi\rangle \otimes |+\hat{x}\rangle$, the scattered wave is $(|\psi_+\rangle\,|+\hat{z}\rangle + |\psi_-\rangle\,|-\hat{z}\rangle)/\sqrt{2}$. We can evaluate the expectation value $\langle\hat{\sigma}_y\rangle$ for the part on the left of the scattering section (including barriers in $\hat{H}_0$) as follows:

$$\langle\hat{\sigma}_Y\rangle = \frac{i\langle\psi_-|f\rangle\langle f|\psi_+\rangle - i\langle\psi_+|f\rangle\langle f|\psi_-\rangle}{|\langle\psi_+|f\rangle|^2 + |\langle\psi_-|f\rangle|^2}. \tag{A4}$$

The problem of 1D scattering has been dealt with in more depth in Ref. [79]. To make a qualitative argument for proportionality to the weak value, we can choose to use the Born approximation. This gives $|\psi_\pm\rangle \approx |\psi\rangle \pm \theta\hat{G}_0\hat{H}_1\,|\psi\rangle$, which then helps to simplify Eq. (A4) to the following form:

$$\begin{aligned}\langle\hat{\sigma}_Y\rangle &= i\theta\frac{\langle\psi|f\rangle\langle f|\hat{G}_0\hat{H}_1|\psi\rangle - \langle\psi|\hat{H}_1\hat{G}_0^\dagger|f\rangle\langle f|\psi\rangle}{\langle\psi|f\rangle\langle f|\psi\rangle + \theta^2\langle\psi|\hat{H}_1\hat{G}_0^\dagger|f\rangle\langle f|\hat{G}_0\hat{H}_1|\psi\rangle} \\ &= -2\theta\,\mathrm{Im}\left(\frac{\langle f|\hat{G}_0\hat{H}_1|\psi\rangle}{\langle f|\psi\rangle}\right) + \mathcal{O}(\theta^2).\end{aligned} \tag{A5}$$

Notably the first-order term is simply the weak value of $\hat{G}_0\hat{H}_1$. To actually evaluate this, we must note that $\hat{H}_1$ is only nonzero in the region of the middle barrier. We can then act the Green's function on $\langle f|$ and we will finally get an integral which is only in the spatial region of the middle barrier as described in Ref. [48].

The form of $\hat{G}_0\hat{H}_1$ for 1D barriers gives us an important insight in the case where the choice of $|\psi\rangle$ which has full transmission (hence maximum $\langle f|\psi\rangle$) results in larger weak values. This case can be observed in the response we obtain for the signal $D_Y = \langle\hat{\sigma}_Y\rangle$.

APPENDIX B: QUANTUM FISHER INFORMATION FOR THE SETUP

In this section, we will work out the expression for the quantum Fisher information which we can obtain out of our resonant tunneling setup. The Hamiltonian is defined in Eq. (A1). We wish to estimate θ to measure Zeeman splitting. This is also a problem that has been studied in the context of quantum walks for 1D scattering [65]. We define the following position Hamiltonians:

$$\hat{H}_0 = \begin{cases} p^2/2m + V_{B1}, & |y| \le d_1/2, \\ p^2/2m + V_{B2}, & d_1/2 < |y| \le d_2/2, \\ p^2/2m, & |y| > d_2/2, \end{cases} \tag{B1}$$

$$\hat{H}_1 = \begin{cases} t_0, & |y| \le d_1/2, \\ 0, & |y| > d_1/2. \end{cases} \tag{B2}$$

For spin-up (or spin-down) particles, the effective Hamiltonian is $\hat{H}_0 + \theta\hat{H}_1$ (or $\hat{H}_0 - \theta\hat{H}_1$). One of the defined Green's function based on the number of particles in the channel is the $\mathbf{G}^n$ function defined in terms of the advanced and retarded Green's functions as $\mathbf{G}^n = \mathbf{G}^r\mathbf{\Sigma}^{\text{in}}\mathbf{G}^a$. We obtain, $\rho = \mathbf{G}^n/\mathrm{Tr}(\mathbf{G}^n)$ and so we can see the following on taking a partial derivative with respect to our parameter:

$$\frac{\partial\mathbf{G}^n}{\partial\theta} = \frac{\partial\mathbf{G}^r}{\partial\theta}\mathbf{\Sigma}^{\text{in}}\mathbf{G}^a + \mathbf{G}^r\mathbf{\Sigma}^{\text{in}}\frac{\partial\mathbf{G}^a}{\partial\theta} + \mathbf{G}^r\frac{\partial\mathbf{\Sigma}^{\text{in}}}{\partial\theta}\mathbf{G}^a. \tag{B3}$$

For the sake of simplicity, we first analyze the case of zero dephasing. In this case, $\mathbf{\Sigma}^{\text{in}}$ only gets contributions from the lesser self-energies of the contacts, as the contribution from Eq. (8) is zero. This means that $\mathbf{\Sigma}^{\text{in}}$ will be independent of θ, since all the θ dependence arises only from $\mathbf{G}^n$ as the contact self-energies have no dependence on the electronic potential. In this case, the retarded Green's function is defined as follows:

$$\begin{aligned}\mathbf{G}^r = [&(E + i\eta)\mathbb{I} - \hat{H}_0 \otimes \mathbb{I}_2 - \theta\hat{H}_1 \\ &\otimes \hat{\sigma}_Z - \mathbf{\Sigma}_L - \mathbf{\Sigma}_R - \mathbf{\Sigma}_{F1} - \mathbf{\Sigma}_{F2}]^{-1}.\end{aligned} \tag{B4}$$

From this we can find the partial derivative of $\mathbf{G}^r$ with respect to the parameter θ:

$$\frac{\partial\mathbf{G}^r}{\partial\theta} = -\hat{H}_1 \times -(\mathbf{G}^r)^2 = \hat{H}_1\mathbf{G}^r \times \mathbf{G}^r. \tag{B5}$$

From the above equation, it follows that

$$\frac{\partial\mathbf{G}^n}{\partial\theta} = (\hat{H}_1\mathbf{G}^r)\mathbf{G}^n + \mathbf{G}^n(\hat{H}_1\mathbf{G}^r)^\dagger. \tag{B6}$$

We must now also account for the fact that $\mathbf{G}^n$ must be normalized to give the expression for the density matrix:

$$\frac{\partial\rho}{\partial\theta} = \frac{\partial}{\partial\theta}\frac{\mathbf{G}^n}{\mathrm{Tr}(\mathbf{G}^n)} = \frac{1}{\mathrm{Tr}(\mathbf{G}^n)}\frac{\partial\mathbf{G}^n}{\partial\theta} - \frac{\mathbf{G}^n}{\mathrm{Tr}(\mathbf{G}^n)^2}\mathrm{Tr}\left(\frac{\partial\mathbf{G}^n}{\partial\theta}\right)$$
$$= \left(\hat{H}_1\mathbf{G}^r - \frac{\mathrm{Tr}((\hat{H}_1\mathbf{G}^r)\mathbf{G}^n)}{\mathrm{Tr}(\mathbf{G}^n)}\mathbb{I}\right)\rho$$
$$+ \rho\left((\hat{H}_1\mathbf{G}^r)^\dagger - \frac{\mathrm{Tr}(\mathbf{G}^n(\hat{H}_1\mathbf{G}^r)^\dagger)}{\mathrm{Tr}(\mathbf{G}^n)}\mathbb{I}\right). \quad \text{(B7)}$$

However, $\mathrm{Tr}(A^\dagger)\mathbb{I} = ((\mathrm{Tr}(A))\mathbb{I})^\dagger$, hence if we define $\tilde{L}$ as

$$\hat{\tilde{L}} = \hat{H}_1\mathbf{G}^r - \frac{\mathrm{Tr}((\hat{H}_1\mathbf{G}^r)\mathbf{G}^n)}{\mathrm{Tr}(\mathbf{G}^n)}\mathbb{I}, \quad \text{(B8)}$$

we can write the following expression:

$$\partial_\theta\rho = \hat{\tilde{L}}\rho + \rho\hat{\tilde{L}}^\dagger. \quad \text{(B9)}$$

This may look a lot like the expression for QFI defined in terms of a symmetric logarithmic derivative (SLD) [17]. The operator $\tilde{L}$ is not Hermitian, hence fails to be an SLD. In general, QFI is defined as the following for density matrix $\rho = \sum\lambda_i\,|i\rangle\,\langle i|$:

$$\mathcal{H} = \sum_{i,j,\lambda_i+\lambda_j\neq 0} 2\mathrm{Re}\frac{\langle i|\partial_\theta\rho|j\rangle\langle j\,|\partial_\theta\rho|i\rangle}{\lambda_i+\lambda_j}. \quad \text{(B10)}$$

To obtain the true SLD we can simply use the matrix elements of $\delta_\theta\rho$ [18]. Here we have $\partial_\theta\rho = \frac{1}{2}(\hat{L}\rho + \rho\hat{L})$. By representing matrix elements using the eigenstates of ρ,

$$\langle i|\hat{L}\rho + \rho\hat{L}|j\rangle = 2(\langle i|\hat{\tilde{L}}\rho + \rho\hat{\tilde{L}}^\dagger|j\rangle), \quad \text{(B11)}$$

$$(\lambda_i+\lambda_j)\langle i|\hat{L}|j\rangle = 2(\lambda_j\langle i|\hat{\tilde{L}}|j\rangle + \lambda_i\langle i|\hat{\tilde{L}}^\dagger|j\rangle), \quad \text{(B12)}$$

$$L = 2\sum_{i,j,\lambda_i+\lambda_j\neq 0}\left(\frac{\lambda_j\langle i|\hat{\tilde{L}}|j\rangle + \lambda_i\langle i|\hat{\tilde{L}}^\dagger|j\rangle}{\lambda_i+\lambda_j}\right) \times |i\rangle\langle j\,|. \quad \text{(B13)}$$

This shows how the operator $\hat{\tilde{L}}$ is directly related to the SLD $\hat{L}$. We can further extend this to the case where dephasing is nonzero. However, similar to the calculation of the Green's functions, their derivatives also have to be found in a self-consistent form. We omit the analytical expressions in this case. Our numerics are carried out by estimation of $\partial_\theta\rho \approx (\rho_{\theta+d\theta} - \rho_\theta)/d\theta$, where $d\theta \ll \theta$. For our simulations, the value of $d\theta$ is set as $\theta/1000$.

APPENDIX C: CURRENT MEASUREMENT AS A STRONG MEASUREMENT

The act of obtaining currents at the ferromagnetic contacts gives the statistics for the spin expectation values. This is due to the fact that the ferromagnetic contact, if aligned along a certain direction, will give a current readout proportional to the population of spins aligned in that particular direction [49]. This can be established in the NEGF formulation. The current readouts are from the FM2 contact at $\pm\hat{y}$ orientation. The current values come out to be as follows:

$$I^{\pm}_{\mathrm{FM2}} = \mathrm{Tr}(\Gamma^{\mathrm{FM2}}\mathbf{G}^n)$$
$$= -2t_0 i\sin(ka)\,\mathrm{Tr}(\mathbf{G}^n)\,\mathrm{Tr}\left(\frac{(\mathbb{I}\pm\hat{\sigma}_y)\delta_{f_2,f_2}}{2}\rho\right). \quad \text{(C1)}$$

The quantity $\mathrm{Tr}((\mathbb{I}\pm\hat{\sigma}_y)\rho/2)$ is simply the probabilities for the POVM set of $\{(\mathbb{I}+\hat{\sigma}_y)/2, (\mathbb{I}-\hat{\sigma}_y)/2\}$. An additional point to note is that our postselection measurement is looking at one point in the whole region which lies to the right of the barrier region (electrons are injected from the left of the barrier). The reason it is only one point is since the current readout only occurs at a specific point in the 1D nanowire. This does not change the expectation value of $\hat{\sigma}_Y$, since this will have to be the same all over the whole region which lies to the right of the barrier region.

Hence, what we use as the expectation value of $\hat{\sigma}_Y$ is the same as the expression we obtain by considering a complete postselected region in Eq. (A4) since the spin part of the wave function is the same everywhere on the right of the barrier. For any 1D scattering problem, all changes only occur at the boundaries. Hence, by looking at one point, we can get the relevant information for the whole postselected region.

APPENDIX D: CLASSICAL FISHER INFORMATION FOR THE SETUP

As we have established previously, we take the current readouts to behave as probabilities for the POVM set of $\{(\mathbb{I}+\hat{\sigma}_y)/2, (\mathbb{I}-\hat{\sigma}_y)/2\}$. Since the state ρ is ultimately dependent on the polarization of FM2 [see Eq. (B4)], the state is slightly different depending on whether it is $+\hat{y}$ or $-\hat{y}$. We first define the probabilities $p_\pm$ as

$$p_\pm = \frac{\mathrm{Tr}(\frac{1}{2}((\mathbb{I}\pm\hat{\sigma}_y)\delta_{f_2,f_2})\mathbf{G}^n_\pm)}{\mathrm{Tr}(\mathbf{G}^n_\pm)}. \quad \text{(D1)}$$

We note that these probabilities are only looking at a certain lattice point corresponding to the contact FM2. Hence we actually need to define conditional properties since those are the actual probabilities we get $\pm\hat{y}$-polarization electrons detected on the other end. Hence let

$\tilde{p}_\pm = p_\pm/(p_+ + p_-)$. From this, the CFI is simply given as follows:

$$\mathcal{H}_c = \tilde{p}_+(\partial_\theta \ln(\tilde{p}_+))^2 + \tilde{p}_-(\partial_\theta \ln(\tilde{p}_-))^2 = \frac{(\partial_\theta \tilde{p}_+)^2}{\tilde{p}_+} + \frac{(\partial_\theta \tilde{p}_-)^2}{\tilde{p}_-}. \tag{D2}$$

This expression can be easily evaluated using Eq. (B6).

While we use this method for calculation of the CFI using the NEGF method, one can also apply the ideas explored in Appendix A here to obtain an expression when the scattering states are pure (zero-dephasing). As stated before, the state obtained after scattering of $|\psi\rangle \otimes |+\hat{x}\rangle$ can be defined as

$$\begin{aligned}|\psi_{\text{scattered}}\rangle &= \frac{1}{\sqrt{2}}(|\psi_+\rangle \otimes |+\hat{z}\rangle + |\psi_-\rangle \otimes |-\hat{z}\rangle) \\ &= \frac{(|\psi_+\rangle - i\,|\psi_-\rangle)}{\sqrt{2}} \otimes |+\hat{y}\rangle \\ &\quad + \frac{(|\psi_+\rangle + i\,|\psi_-\rangle)}{\sqrt{2}} \otimes |-\hat{y}\rangle.\end{aligned} \tag{D3}$$

The projection for probabilities of $\hat{y}$ spin measurement will be over the state $|f\rangle \otimes |\pm\hat{y}\rangle$, giving

$$p'_\pm = \frac{|\langle f \mid \psi_+\rangle \mp i\langle f \mid \psi_-\rangle|^2}{2}. \tag{D4}$$

We can now employ the Born approximation expression of $|\psi_\pm\rangle = |\psi\rangle \pm \theta \hat{G}_0 \hat{H}_0 |\psi\rangle$. Using this we obtain

$$\frac{\partial(\ln(p'_\pm))}{\partial\theta} = \frac{1}{p'_\pm}\frac{\partial(p'_\pm)}{\partial\theta} = \pm 2\text{Im}\left(\frac{\langle f\,|\hat{G}_0\hat{H}_0|\psi\rangle}{\langle f \mid \psi\rangle}\right) + \mathcal{O}(\theta^2). \tag{D5}$$

From Eq. (D2) we can see how a large value of $\partial_\theta(\ln(p'_\pm))$ will clearly result in a large value of $\mathcal{H}_c$. This in turn implies a smaller variance for estimation of θ.

[1] V. Giovannetti, S. Lloyd, and L. Maccone, Quantum metrology, Phys. Rev. Lett. **96**, 010401 (2006).

[2] V. Giovannetti, S. Lloyd, and L. Maccone, Advances in quantum metrology, Nat. Photonics **5**, 222 (2011).

[3] C. Degen, F. Reinhard, and P. Cappellaro, Quantum sensing, Rev. Mod. Phys. **89**, 035002 (2017).

[4] E. Polino, M. Valeri, N. Spagnolo, and F. Sciarrino, Photonic quantum metrology, AVS Quantum Sci. **2**, 024703 (2020).

[5] M. A. Taylor and W. P. Bowen, Quantum metrology and its application in biology, Phys. Rep. **615**, 1 (2016).

[6] J. Joo, W. J. Munro, and T. P. Spiller, Quantum metrology with entangled coherent states, Phys. Rev. Lett. **107**, 083601 (2011).

[7] S. Pang and T. A. Brun, Quantum metrology for a general Hamiltonian parameter, Phys. Rev. A **90**, 022117 (2014).

[8] R. Kaubruegger, D. V. Vasilyev, M. Schulte, K. Hammerer, and P. Zoller, Quantum variational optimization of Ramsey interferometry and atomic clocks, Phys. Rev. X **11**, 041045 (2021).

[9] C. D. Marciniak, T. Feldker, I. Pogorelov, R. Kaubruegger, D. V. Vasilyev, R. van Bijnen, P. Schindler, P. Zoller, R. Blatt, and T. Monz, Optimal metrology with programmable quantum sensors, Nature **603**, 604 (2022).

[10] H. F. Hofmann, Uncertainty limits for quantum metrology obtained from the statistics of weak measurements, Phys. Rev. A **83**, 022106 (2011).

[11] A. G. Kofman, S. Ashhab, and F. Nori, Nonperturbative theory of weak pre- and post-selected measurements, Phys. Rep. **520**, 43 (2012).

[12] J. Dressel and A. N. Jordan, Weak values are universal in Von Neumann measurements, Phys. Rev. Lett. **109**, 230402 (2012).

[13] K. Lyons, J. Dressel, A. N. Jordan, J. C. Howell, and P. G. Kwiat, Power-recycled weak-value-based metrology, Phys. Rev. Lett. **114**, 170801 (2015).

[14] G. I. Viza, J. Martínez-Rincón, G. B. Alves, A. N. Jordan, and J. C. Howell, Experimentally quantifying the advantages of weak-value-based metrology, Phys. Rev. A **92**, 032127 (2015).

[15] L. Xu, Z. Liu, A. Datta, G. C. Knee, J. S. Lundeen, Y.-q. Lu, and L. Zhang, Approaching quantum-limited metrology with imperfect detectors by using weak-value amplification, Phys. Rev. Lett. **125**, 080501 (2020).

[16] Y. Liu, L. Qin, and X.-Q. Li, Fisher information analysis on weak-value-amplification metrology using optical coherent states, Phys. Rev. A **106**, 022619 (2022).

[17] J. Liu, H. Yuan, X.-M. Lu, and X. Wang, Quantum Fisher information matrix and multiparameter estimation, J. Phys. A: Math. Theor. **53**, 023001 (2019).

[18] M. G. Paris, Quantum estimation for quantum technology, Int. J. Quantum Inf. **7**, 125 (2009).

[19] P. Facchi, R. Kulkarni, V. Man'ko, G. Marmo, E. Sudarshan, and F. Ventriglia, Classical and quantum Fisher information in the geometrical formulation of quantum mechanics, Phys. Lett. A **374**, 4801 (2010).

[20] A. Fujiwara and H. Nagaoka, Quantum Fisher metric and estimation for pure state models, Phys. Lett. A **201**, 119 (1995).

[21] G. B. Alves, B. M. Escher, R. L. de Matos Filho, N. Zagury, and L. Davidovich, Weak-value amplification as an optimal metrological protocol, Phys. Rev. A **91**, 062107 (2015).

[22] L. Vaidman, Weak value controversy, Philos. Trans. R. Soc. A: Math. Phys. Eng. Sci. **375**, 20160395 (2017).

[23] P. B. Dixon, D. J. Starling, A. N. Jordan, and J. C. Howell, Ultrasensitive beam deflection measurement via interferometric weak value amplification, Phys. Rev. Lett. **102**, 173601 (2009).

[24] C. Ferrie and J. Combes, Weak value amplification is suboptimal for estimation and detection, Phys. Rev. Lett. **112**, 040406 (2014).

[25] J. Combes, C. Ferrie, Z. Jiang, and C. M. Caves, Quantum limits on postselected, probabilistic quantum metrology, Phys. Rev. A **89**, 052117 (2014).

[26] A. N. Jordan, J. Martínez-Rincón, and J. C. Howell, Technical advantages for weak-value amplification: When less is more, Phys. Rev. X **4**, 011031 (2014).
[27] G. C. Knee, J. Combes, C. Ferrie, and E. M. Gauger, Weak-value amplification: State of play, Quantum Meas. Quantum Metrology **3**, 32 (2016).
[28] M. Vetrivelan and S. Vinjanampathy, Near-deterministic weak-value metrology via collective non-linearity, Quantum Sci. Technol. **7**, 025012 (2022).
[29] T. Jullien, P. Roulleau, B. Roche, A. Cavanna, Y. Jin, and D. C. Glattli, Quantum tomography of an electron, Nature **514**, 603 (2014).
[30] P. Samuelsson and M. Büttiker, Quantum state tomography with quantum shot noise, Phys. Rev. B **73**, 041305 (2006).
[31] M. Tam, C. Flindt, and F. Brange, Optimal entanglement witness for Cooper pair splitters, Phys. Rev. B **104**, 245425 (2021).
[32] A. Ranni, F. Brange, E. T. Mannila, C. Flindt, and V. F. Maisi, Real-time observation of Cooper pair splitting showing strong non-local correlations, Nat. Commun. **12**, 6358 (2021).
[33] S. E. Nigg, R. P. Tiwari, S. Walter, and T. L. Schmidt, Detecting nonlocal Cooper pair entanglement by optical Bell inequality violation, Phys. Rev. B **91**, 094516 (2015).
[34] F. Brange, K. Prech, and C. Flindt, Dynamic Cooper pair splitter, Phys. Rev. Lett. **127**, 237701 (2021).
[35] R. S. Deacon, A. Oiwa, J. Sailer, S. Baba, Y. Kanai, K. Shibata, K. Hirakawa, and S. Tarucha, Cooper pair splitting in parallel quantum dot Josephson junctions, Nat. Commun. **6**, 7446 (2015).
[36] W. Pfaff, T. H. Taminiau, L. Robledo, H. Bernien, M. Markham, D. J. Twitchen, and R. Hanson, Demonstration of entanglement-by-measurement of solid-state qubits, Nat. Phys. **9**, 29 (2013).
[37] R. Ionicioiu, P. Zanardi, and F. Rossi, Testing Bell's inequality with ballistic electrons in semiconductors, Phys. Rev. A **63**, 050101 (2001).
[38] A. Bednorz and W. Belzig, Proposal for a cumulant-based Bell test for mesoscopic junctions, Phys. Rev. B **83**, 125304 (2011).
[39] B. T. Zhou, K. Taguchi, Y. Kawaguchi, Y. Tanaka, and K. T. Law, Spin-orbit coupling induced valley Hall effects in transition-metal dichalcogenides, Commun. Phys. **2**, 26 (2019).
[40] Y. Zhang, Z. Hou, Y.-X. Zhao, Z.-H. Guo, Y.-W. Liu, S.-Y. Li, Y.-N. Ren, Q.-F. Sun, and L. He, Correlation-induced valley splitting and orbital magnetism in a strain-induced zero-energy flatband in twisted bilayer graphene near the magic angle, Phys. Rev. B **102**, 081403 (2020).
[41] Y. Li, J. Ludwig, T. Low, A. Chernikov, X. Cui, G. Arefe, Y. D. Kim, A. M. van der Zande, A. Rigosi, H. M. Hill, S. H. Kim, J. Hone, Z. Li, D. Smirnov, and T. F. Heinz, Valley splitting and polarization by the Zeeman effect in monolayer $MoSe_2$, Phys. Rev. Lett. **113**, 266804 (2014).
[42] X.-X. Zhang, Y. Lai, E. Dohner, S. Moon, T. Taniguchi, K. Watanabe, D. Smirnov, and T. F. Heinz, Zeeman-induced valley-sensitive photocurrent in monolayer MoS_2, Phys. Rev. Lett. **122**, 127401 (2019).
[43] A. Dankert and S. P. Dash, Electrical gate control of spin current in van der Waals heterostructures at room temperature, Nat. Commun. **8**, 16093 (2017).
[44] D. Khokhriakov, A. M. Hoque, B. Karpiak, and S. P. Dash, Gate-tunable spin-galvanic effect in graphene-topological insulator van der Waals heterostructures at room temperature, Nat. Commun. **11**, 3657 (2020).
[45] M. V. Kamalakar, A. Dankert, P. J. Kelly, and S. P. Dash, Inversion of spin signal and spin filtering in ferromagnet—hexagonal boron nitride-graphene van der Waals heterostructures, Sci. Rep. **6**, 21168 (2016).
[46] E. Tsitsishvili, G. S. Lozano, and A. O. Gogolin, Rashba coupling in quantum dots: An exact solution, Phys. Rev. B **70**, 115316 (2004).
[47] J. C. R. Sánchez, L. Vila, G. Desfonds, S. Gambarelli, J. P. Attané, J. M. De Teresa, C. Magén, and A. Fert, Spin-to-charge conversion using Rashba coupling at the interface between non-magnetic materials, Nat. Commun. **4**, 2944 (2013).
[48] A. M. Steinberg, How much time does a tunneling particle spend in the barrier region?, Phys. Rev. Lett. **74**, 2405 (1995).
[49] A. Mathew, K. Y. Camsari, and B. Muralidharan, Proposal for a solid-state magnetoresistive Larmor quantum clock, Phys. Rev. B **105**, 144418 (2022).
[50] B. Ricco and M. Y. Azbel, Physics of resonant tunneling. The one-dimensional double-barrier case, Phys. Rev. B **29**, 1970 (1984).
[51] J. P. Sun, G. Haddad, P. Mazumder, and J. Schulman, Resonant tunneling diodes: Models and properties, Proc. IEEE **86**, 641 (1998).
[52] M. T. Björk, B. J. Ohlsson, C. Thelander, A. I. Persson, K. Deppert, L. R. Wallenberg, and L. Samuelson, Nanowire resonant tunneling diodes, Appl. Phys. Lett. **81**, 4458 (2002).
[53] P. Mazumder, S. Kulkarni, M. Bhattacharya, J. P. Sun, and G. Haddad, Digital circuit applications of resonant tunneling devices, Proc. IEEE **86**, 664 (1998).
[54] P. Danielewicz, Quantum theory of nonequilibrium processes, i, Ann. Phys. **152**, 239 (1984).
[55] S. Datta, *Electronic Transport in Mesoscopic Systems* (Cambridge University Press, Cambridge UK, 1997).
[56] S. Datta, *Quantum Transport: Atom to Transistor* (Cambridge University Press, Cambridge UK, 2005), 2nd ed.
[57] R. Golizadeh-Mojarad and S. Datta, Nonequilibrium Green's function based models for dephasing in quantum transport, Phys. Rev. B **75**, 081301 (2007).
[58] A. Sharma, A. Tulapurkar, and B. Muralidharan, Ultrasensitive nanoscale magnetic-field sensors based on resonant spin filtering, IEEE Trans. Electron Devices **63**, 4527 (2016).
[59] A. Sharma, A. A. Tulapurkar, and B. Muralidharan, Bandpass Fabry-Pèrot magnetic tunnel junctions, Appl. Phys. Lett. **112**, 192404 (2018).
[60] A. Singha and B. Muralidharan, Performance analysis of nanostructured Peltier coolers, J. Appl. Phys. **124**, 144901 (2018).
[61] A. Sharma, A. A. Tulapurkar, and B. Muralidharan, Resonant spin-transfer-torque nano-oscillators, Phys. Rev. Appl. **8**, 064014 (2017).
[62] K. Y. Camsari, S. Chowdhury, and S. Datta, in *Springer Handbook of Semiconductor Devices*, edited by M. Rudan, R. Brunetti, and S. Reggiani (Springer International Publishing, Cham, 2023), p. 1583.

[63] C. Duse, P. Sriram, K. Gharavi, J. Baugh, and B. Muralidharan, Role of dephasing on the conductance signatures of Majorana zero modes, J. Phys.: Condens. Matter **33**, 365301 (2021).
[64] M. Büttiker, Larmor precession and the traversal time for tunneling, Phys. Rev. B **27**, 6178 (1983).
[65] F. Zatelli, C. Benedetti, and M. G. A. Paris, Scattering as a quantum metrology problem: A quantum walk approach, Entropy **22**, 1321 (2020).
[66] J. J. Sakurai and J. Napolitano, *Modern Quantum Mechanics* (Cambridge University Press, Cambridge UK, 2017), 2nd ed.
[67] J. Dressel, M. Malik, F. M. Miatto, A. N. Jordan, and R. W. Boyd, Colloquium: Understanding quantum weak values: Basics and applications, Rev. Mod. Phys. **86**, 307 (2014).
[68] I. M. Duck, P. M. Stevenson, and E. C. G. Sudarshan, The sense in which a "weak measurement" of a spin-1/2 particle's spin component yields a value 100, Phys. Rev. D **40**, 2112 (1989).
[69] Y. Meir and N. S. Wingreen, Landauer formula for the current through an interacting electron region, Phys. Rev. Lett. **68**, 2512 (1992).
[70] H. Haug and A. Jauho, *Quantum Kinetics in Transport and Optics of Semiconductors*, Springer Series in Solid-State Sciences (Springer, Berlin Heidelberg, 2007).
[71] J. Liu, J. Chen, X.-X. Jing, and X. Wang, Quantum Fisher information and symmetric logarithmic derivative via anti-commutators, J. Phys. A: Math. Theor. **49**, 275302 (2016).
[72] S. Boixo, S. T. Flammia, C. M. Caves, and J. Geremia, Generalized limits for single-parameter quantum estimation, Phys. Rev. Lett. **98**, 090401 (2007).
[73] S. L. Braunstein, C. M. Caves, and G. Milburn, Generalized uncertainty relations: Theory, examples, and Lorentz invariance, Ann. Phys. **247**, 135 (1996).
[74] G. S. Agarwal and L. Davidovich, Quantifying quantum-amplified metrology via Fisher information, Phys. Rev. Res. **4**, L012014 (2022).
[75] R. Demkowicz-Dobrzański, J. Kołodyński, and M. GuŢă, The elusive Heisenberg limit in quantum-enhanced metrology, Nat. Commun. **3**, 1063 (2012).
[76] M. Zwierz, C. A. Pérez-Delgado, and P. Kok, Ultimate limits to quantum metrology and the meaning of the Heisenberg limit, Phys. Rev. A **85**, 042112 (2012).
[77] M. Zwierz, C. A. Pérez-Delgado, and P. Kok, General optimality of the Heisenberg limit for quantum metrology, Phys. Rev. Lett. **105**, 180402 (2010).
[78] A. Lahiri, K. Gharavi, J. Baugh, and B. Muralidharan, Nonequilibrium Green's function study of magnetoconductance features and oscillations in clean and disordered nanowires, Phys. Rev. B **98**, 125417 (2018).
[79] Y. Aharonov and L. Vaidman, in *Time in Quantum Mechanics*, edited by J. Muga, R. S. Mayato, and Í. Egusquiza (Springer, Berlin, Heidelberg, 2008), p. 399.